INTERNATIONAL JOURNAL FOR NUMERICAL METHODS IN FLUIDS, VOL. 25, 847–857 (1997)

# NUMERICAL MODELLING OF SHEAR-DEPENDENT MASS TRANSFER IN LARGE ARTERIES

GERHARD RAPPITSCH,* KARL PERKTOLD AND ELISABETH PERNKOPF

*Institute of Mathematics, Technical University of Graz, Steyrergasse 30/3, A-8010 Graz, Austria*

## SUMMARY

A numerical scheme for the simulation of blood flow and transport processes in large arteries is presented. Blood flow is described by the unsteady 3D incompressible Navier–Stokes equations for Newtonian fluids; solute transport is modelled by the advection–diffusion equation. The resistance of the arterial wall to transmural transport is described by a shear-dependent wall permeability model. The finite element formulation of the Navier–Stokes equations is based on an operator-splitting method and implicit time discretization. The streamline upwind/Petrov–Galerkin (SUPG) method is applied for stabilization of the advective terms in the transport equation and in the flow equations. A numerical simulation is carried out for pulsatile mass transport in a 3D arterial bend to demonstrate the influence of arterial flow patterns on wall permeability characteristics and transmural mass transfer. The main result is a substantial wall flux reduction at the inner side of the curved region. © 1997 John Wiley & Sons, Ltd.

*Int. J. Numer. Meth. Fluids*, **25**: 847–857, 1997.

No. of Figures: 5. No. of Tables: 0. No. of References: 27.

KEY WORDS: finite element method; blood flow; arterial transport processes; curved tubes

## 1. INTRODUCTION

Cardiovascular transport mechanisms are important in the development of atherosclerosis, a slowly progressive, occlusive disease of large- and medium-size arteries. Of particular interest are the transport processes of macromolecules (albumin, LDL) and dissolved gases ($O_2$, $CO_2$) in the arterial lumen and through the arterial wall. Both processes are coupled and strongly influenced by local blood flow patterns. The luminal mass transport is a highly convection-dominated process owing to the low diffusivity of the interesting substances. The mass transfer through the arterial wall can be defined as the flux through a biological membrane whose permeability depends strongly on fluid dynamic factors, especially on the wall shear stress.[1] Thus a model describing arterial mass transfer must be capable of treating simultaneously the solute transport in the blood phase as well as shear-dependent variations in wall permeability. The influence of arterial fluid dynamics on the development of atherosclerotic lesions was analysed in a number of numerical[2–4] and experimental[5]

* Correspondence to: G. Rappitsch, Institute of Mathematics, Technical University Graz, Steyrergasse 30/3, A-8010 Graz, Austria.

Contract grant sponsor: Austrian Science Foundation. Contract grant number: P 10494 TEC.

CCC 0271–2091/97/070829–11 $17.50

*Received June 1996*
*Revised November 1996*

studies. According to recent findings, fluid dynamic factors such as flow separation, flow recirculation and low and oscillating wall shear stress may contribute to the progression of the disease.[5] However, relatively few numerical studies have been carried out to examine the way in which special flow patterns affect luminal and transmural transport processes.[6–8]

In the present study a numerical scheme for the simulation of arterial transport processes is presented. The mathematical description of blood flow uses the time-dependent Navier–Stokes equations for incompressible Newtonian fluids; the transport of macromolecules and gases is described by the advection–diffusion equation. The concept of shear-dependent wall permeability is included in the boundary conditions of the advection–diffusion equation in the form of a passive transport law for the diffusive flux. The numerical calculation of the flow equations and the highly convection-dominated transport equation uses the streamline upwind/Petrov-Galerkin (SUPG)[9–11] technique and implicit time integration. The finite element formulations for the Navier–Stokes equations apply a pressure–velocity correction method[3,12,13] (projection method).

Numerical results are presented for pulsatile flow and arterial mass transport in a 3D curved tube model simulating an arterial bend. Since atherosclerotic lesions tend to occur in regions of branching and sharp curvature, this is a segment of physiological interest. The physical parameters were chosen to match the conditions for oxygen transport in large arteries. Since local hypoxia may accelerate atherosclerotic processes,[14] oxygen transport studies are of clinical interest.

## 2. GOVERNING EQUATIONS

Arterial blood flow is described by the time-dependent Navier–Stokes equations for incompressible Newtonian fluids in non-dimensional form

$$\begin{aligned} \frac{\partial \mathbf{u}}{\partial t} + (\mathbf{u}\cdot\nabla)\mathbf{u} - \frac{1}{Re}\nabla^2\mathbf{u} + \nabla P = 0 \quad &\text{in } \Omega, \\ \nabla\cdot\mathbf{u} = 0 \quad &\text{in } \Omega, \end{aligned} \tag{1}$$

where $\mathbf{u}$ is the velocity vector, $P$ is the pressure and $Re$ is the Reynolds number. The transport of solutes is governed by the transient advection–diffusion equation

$$\frac{\partial C}{\partial t} + \mathbf{u}\cdot\nabla C - \frac{1}{Pe}\nabla^2 C = 0 \quad \text{in } \Omega, \tag{2}$$

where $C$ is the solute concentration and $Pe$ is the Peclet number. The definitions of the non-dimensional parameters are

$$Re = U_0 L_0/\nu, \qquad Pe = U_0 L_0/D, \tag{3}$$

where $U_0$ is the characteristic velocity, $L_0$ is the characteristic length (inlet diameter), $\nu$ is the kinematic viscosity and $D$ is the constant diffusion coefficient.

For the flow problem of interest here the flow partitions into two sections with different types of boundary conditions. At one boundary section (flow entrance and vessel wall) the flow velocity is prescribed:

$$\mathbf{u} = \mathbf{g} \quad \text{on } \Gamma_1. \tag{4}$$

At the remaining boundary section (outflow boundary) a zero surface traction force is assumed:

$$\left(-p\mathbf{I} + \frac{1}{Re}(\nabla\mathbf{u} + \nabla\mathbf{u}^{\mathrm{T}})\right)\mathbf{n} = 0 \quad \text{on } \Gamma_2, \tag{5}$$

 

where $\mathbf{n}$ is the outward-pointing normal vector on $\Gamma_2$. As initial condition a divergence-free velocity field $\mathbf{u}_0(\mathbf{x})$ is specified over the domain $\Omega$ at $t=0$:

$$\mathbf{u}(\mathbf{x}, 0) = \mathbf{u}_0(\mathbf{x}) \quad \text{in } \Omega. \tag{6}$$

For the advection–diffusion equation a constant concentration is assumed at the flow entrance (boundary $\Gamma_D$) and an initial concentration is prescribed at $t=0$:

$$C = C_{\mathrm{D}} \quad \text{on } \Gamma_{\mathrm{D}}, \qquad C(\mathbf{x}, 0) = C_0(\mathbf{x}) \quad \text{in } \Omega. \tag{7}$$

At the wall (boundary $\Gamma_{\mathrm{N}}$) a constitutive relation for the diffusive flux $q_{\mathrm{w}}$ is prescribed:

$$q_{\mathrm{w}} = -D\frac{\partial C}{\partial \mathbf{n}} = \alpha_{\mathrm{w}} C \quad \text{on } \Gamma_{\mathrm{N}}. \tag{8}$$

The wall permeability $\alpha_{\mathrm{w}}$ is assumed to be a function of the local wall-shear stress magnitude $\|\tau_{\mathrm{w}}\|$. The shear stress vector at the wall is defined by

$$\boldsymbol{\tau}_{\mathrm{w}} = -\mu \left.\frac{\partial \mathbf{u}_{\mathrm{t}}}{\partial \mathbf{n}}\right|_{\mathrm{wall}}, \tag{9}$$

where $\mathbf{u}_{\mathrm{t}}$ is the tangential velocity and $\mu$ is the dynamic viscosity. In the present study the wall permeability is assumed to be linearly dependent on $\|\boldsymbol{\tau}_{\mathrm{w}}\|$:

$$\alpha_{\mathrm{w}} = \beta\|\boldsymbol{\tau}_{\mathrm{w}}\|, \quad \beta \text{ constant}. \tag{10}$$

## 3. FINITE ELEMENT FORMULATIONS

### *3.1. Navier–Stokes equations*

The numerical algorithm for the Navier–Stokes problem is based on a fractional step method (projection method) originally proposed by Chorin[15] in the finite difference context. Applications of Chorin's approach to finite elements have been reported in References 16 and 17. The present method[3,12,13] uses a mathematical theorem which allows the decomposition of a sufficiently regular vector field into a divergence-free field and an irrotational field.[18,19] This theorem can be applied to the variational formulation of the Navier–Stokes equations in the appropriate function spaces.[18,19] Introducing an auxiliary vector field $\tilde{\mathbf{u}}^{n+1}$ and using implicit time integration, the variational form of the Navier–Stokes equations can be written as

$$\frac{1}{\Delta t}\int_\Omega (\tilde{\mathbf{u}}^{n+1} - \mathbf{u}^n)\psi \,\mathrm{d}x + \int_\Omega (\tilde{\mathbf{u}}^{n+1}\cdot\nabla)\tilde{\mathbf{u}}^{n+1}\psi \,\mathrm{d}x + \frac{1}{Re}\int_\Omega \nabla\tilde{\mathbf{u}}^{n+1}\psi \,\mathrm{d}x$$
$$-\int_\Omega P^n\nabla\psi \,\mathrm{d}x = \int_{\Gamma_2}\frac{\partial\tilde{\mathbf{u}}^{n+1}}{\partial\mathbf{n}}\psi \,\mathrm{d}s - \int_\Gamma P^n\psi\mathbf{n}\,\mathrm{d}s, \quad \forall\psi \in (H^1(\Omega))^3 \wedge \psi|_{\Gamma_1} = 0, \tag{11}$$

$$\frac{1}{\Delta t}\int_\Omega (\mathbf{u}^{n+1} - \tilde{\mathbf{u}}^{n+1})\psi \,\mathrm{d}x - \int_\Omega (P^{n+1} - P^n)\nabla\psi \,\mathrm{d}x = 0, \quad \forall\psi \in (H^1(\Omega))^3 \wedge \psi|_{\Gamma_1} = 0, \tag{12}$$

$$\int_\Omega \nabla\cdot\mathbf{u}^{n+1}\vartheta \,\mathrm{d}x = 0, \quad \forall\vartheta \in L_2(\Omega). \tag{13}$$

Equations (12) and (13) are approximated using the standard Galerkin finite element method. For stabilization of the advective terms an SUPG formulation[9,10] is applied to equation (11). The spatial

 

discretization uses isoparametric brick elements with trilinear velocity approximation and constant pressure. The finite element approximation on an element level is defined by

$$\mathbf{u}^e(\mathbf{x};t)=\sum_{i=1}^{8} N_i\mathbf{u}_i^e(t), \qquad P^e(\mathbf{x};t)=MP_{\mathrm{c}}^e(t), \tag{14}$$

where $N_i$, $i=1,\ldots,8$, $M$ are the interpolation functions for the velocity components and the pressure ($M=1$); $\mathbf{u}_i^e$, $i=1,\ldots,8$, and $P_{\mathrm{c}}^e$ are the unknown velocity node values (eight corner nodes) and the unknown pressure element centre value. The non-linear convection terms are linearized and Picard iteration is applied. Let $\mathbf{u}^n$ and $P^n$ denote the velocity node values and pressure element values of the preceding time step $t^n$. Then the following calculation algorithm results for $\mathbf{u}^{n+1,m+1}$ and $P^{n+1,m+1}$ at time level $n+1$ and Picard iteration level $m+1$.

1. Calculate the auxiliary velocity vector field $\tilde{\mathbf{u}}^{n+1,m+1}$ from the linearized system

$$\left[(\mathbf{M}+\tilde{\mathbf{M}}^{n+1,m})+\Delta t\left(\mathbf{K}(\mathbf{u}^{n+1,m})+\tilde{\mathbf{K}}^{n+1,m}+\frac{1}{Re}\mathbf{L}\right)\right]\tilde{\mathbf{u}}^{n+1,m+1} = (\mathbf{M}+\tilde{\mathbf{M}}^{n+1,m})\mathbf{u}^n+\Delta t\mathbf{Q}P^{n+1,m}+\mathbf{f}^{n+1}. \tag{15}$$

2. Calculate the pressure correction $q^{n+1,m+1}=P^{n+1,m+1}-P^{n+1,m}$:

$$\mathbf{Q}^{\mathrm{T}}\mathbf{M}_{\mathrm{d}}^{-1}\mathbf{Q}q^{n+1,m+1}=-\frac{1}{\Delta t}\mathbf{Q}^{\mathrm{T}}\tilde{\mathbf{u}}^{n+1,m+1}. \tag{16}$$

3. Calculate the divergence-free velocity field $\mathbf{u}^{n+1,m+1}$:

$$\mathbf{u}^{n+1,m+1}=\tilde{\mathbf{u}}^{n+1,m+1}+\Delta t\mathbf{M}_{\mathrm{d}}^{-1}\mathbf{Q}q^{n+1,m+1}. \tag{17}$$

4. Calculate the updated pressure $P^{n+1,m+1}$:

$$P^{n+1,m+1}=P^{n+1,m}+q^{n+1,m+1}. \tag{18}$$

In the equation system (15)–(18) for the velocity and the pressure, $\mathbf{M}$ is the mass matrix, $M_{\mathrm{d}}$ is the lumped mass matrix, $\mathbf{K}(\mathbf{u}^{n+1,m})$ is the convection matrix, $\mathbf{L}$ is the diffusion matrix, $\mathbf{Q}=(\mathbf{Q}^x,\mathbf{Q}^y,\mathbf{Q}^z)^{\mathrm{T}}$ is the gradient matrix and $\mathbf{f}^{n+1}$ is the vector containing the prescribed boundary conditions. The matrices $\tilde{\mathbf{M}}^{n+1,m}$ and $\tilde{\mathbf{K}}^{n+1,m}$ result from the additional weighting of (11) according to the Petrov–Galerkin formulation.[9] The components of the matrices at the finite element level are defined as

$$M_{ij}=\int_{\Omega_e} N_iN_j\,\mathrm{d}e, \qquad K_{ij}=\int_{\Omega_e} N_i(\mathbf{u}^{n+1,m}\cdot\nabla N_j)\,\mathrm{d}e, \qquad L_{ij}=\int_{\Omega_e}\nabla N_i\cdot\nabla N_j\,\mathrm{d}e, \tag{19}$$

$$Q_{ik}^x=\int_{\Omega_e}\frac{\partial N_i}{\partial x}M_k\,\mathrm{d}e, \qquad Q_{ik}^y=\int_{\Omega_e}\frac{\partial N_i}{\partial y}M_k\,\mathrm{d}e, \qquad Q_{ik}^z=\int_{\Omega_e}\frac{\partial N_i}{\partial z}M_k\,\mathrm{d}e. \tag{20}$$

The components of $\tilde{\mathbf{M}}^{n+1,m}$ and $\tilde{\mathbf{K}}^{n+1,m}$ resulting from the additional weighting of (11) with the upwind perturbation term $\tilde{p}^{n+1,m}=\tilde{k}^{n+1,m}\mathbf{u}^{n+1,m}\cdot\nabla N_i/\|\mathbf{u}^{n+1,m}\|^2$ are defined by

$$\tilde{M}_{ij}^{n+1,m}=\int_{\Omega_e}\frac{\tilde{k}^{n+1,m}}{\|\mathbf{u}^{n+1,m}\|^2}(\mathbf{u}^{n+1,m}\cdot\nabla N_i)N_j\,\mathrm{d}e. \tag{21}$$

$$\tilde{K}_{ij}^{n+1,m}=\int_{\Omega_e}\frac{\tilde{k}^{n+1,m}}{\|\mathbf{u}^{n+1,m}\|^2}(\mathbf{u}^{n+1,m}\cdot\nabla N_i)(\mathbf{u}^{n+1,m}\cdot\nabla N_j)\,\mathrm{d}e. \tag{22}$$

 

Owing to the linear interpolation functions used, there is no contribution from the additional weighting of the diffusive term. The upwind parameter $\tilde{k}^{n+1,m} = \tilde{k}^{n+1,m}(Pe_h^{n+1,m})$ is determined according to Hughes *et al.*[11] as a function of the local element Peclet numbers $Pe_h^{n+1,m} = Re\|\mathbf{u}^{n+1,m}\|h/2$. The Navier–Stokes solver described has been validated with many examples.[13,20] Applications to 3D unsteady flow problems have been performed by Perktold and coworkers,[2–4] where the developed algorithm has been applied to the simulation of non-Newtonian inelastic blood flow[2] and to the flow in arteries with elastic walls.[3,4]

### 3.2. Transport equation

Applying implicit time discretization, the variational form of the advection–diffusion equation subject to the boundary conditions (7) and (8) is

$$\frac{1}{\Delta t}\int_\Omega (C^{n+1} - C^n)\phi \, \mathrm{d}x + \int_\Omega \mathbf{u}^{n+1} \cdot \nabla C^{n+1}\phi \, \mathrm{d}x + \int_\Omega \frac{1}{Pe}\nabla C^{n+1} \cdot \nabla\phi \, \mathrm{d}x = -\int_{\Gamma_N} \frac{1}{Pe}\alpha_w C^{n+1}\phi \, \mathrm{d}s, \quad \forall\phi \in H^1(\Omega) \wedge \phi|_{\Gamma_D} = 0. \tag{23}$$

Using eight-node brick elements and trilinear interpolation functions for the concentration

$$C^e(\mathbf{x}; t) = \sum_{i=1}^{8} N_i c_i^e(t), \tag{24}$$

the algebraic system relating from the SUPG formulation of (23) is

$$\left[(\mathbf{M} + \tilde{\mathbf{M}}^{n+1}) + \Delta t\left((\mathbf{K} + \tilde{\mathbf{K}}^{n+1}) + \frac{1}{Pe}(\mathbf{L} + \mathbf{R})\right)\right]\mathbf{c}^{n+1} = (\mathbf{M} + \tilde{\mathbf{M}}^{n+1})\mathbf{c}^n + \mathbf{f}^{n+1}. \tag{25}$$

The components of the matrices $\mathbf{M}, \mathbf{K}, \mathbf{L}$ and $\tilde{\mathbf{M}}(\mathbf{u}^{n+1}), \tilde{\mathbf{K}}(\mathbf{u}^{n+1})$ are defined according to (19)–(22), where the upwind parameter $\tilde{k}^{n+1}$ is based on the local element Peclet number $Pe_h^{n+1} = Pe\|\mathbf{u}^{n+1}\|h/2$. The matrix $\mathbf{R}$ results from the consideration of the boundary integral in (23) and its components on an element level are defined for neighbouring nodes $i', j' \in \Gamma_N$ by

$$R_{i'j'} = \int_{\gamma_N^e} \alpha_w N_{i'} N_{j'} \, \mathrm{d}s, \tag{26}$$

where the permeability function $\alpha_w$ is determined according to (10). Validation studies of the described calculation algorithm for the unsteady transport equation have been performed.[21] The presented numerical solution methods for the Navier–Stokes equations (15)–(18) and the advection–diffusion equation (25) have been applied to the calculation of coupled flow and oxygen transport[8] and to the simulation of shear-dependent protein transport in axisymmetric domains.[22]

## 4. NUMERICAL RESULTS AND DISCUSSION

A numerical simulation of pulsatile blood flow and arterial mass transport in a 3D 90° curved tube artery model (Figure 1) is carried out. The parameters (diffusion coefficient, permeability) were chosen to model physiological conditions for the transport of dissolved oxygen. The physical dimensions are: tube diameter, $L_0 = 0{\cdot}62$ cm; length of inlet section, $L_{en} = 2L_0$; length of outlet section, $L_{out} = 10L_0$; radius of curvature, $R = 0{\cdot}62$ cm. The computer simulation is carried out under

 

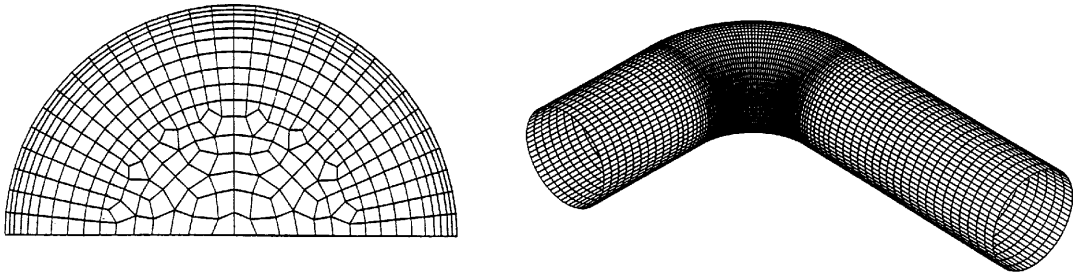

Figure 1. Curved tube artery model: finite element subdivision at a cross-section and in curved region

pulsatile flow conditions simulating arterial flow.[4] A sinusoidal wave-form is used for the averaged axial velocity at the entrance:

$$\overline{u_{\text{in}}}(t) = U_0[1 - \cos(\omega t)], \tag{27}$$

where $U_0 = 16{\cdot}9\,\text{cm}\,\text{s}^{-1}$ is the time-averaged mean inlet velocity and $\omega = 8{\cdot}38$ is the angular frequency based on a pulse period $T_\text{p} = 0{\cdot}75$ s. Fully developed inlet velocity profiles corresponding to the chosen pulse wave-form (Womersley solutions) are numerically calculated as long straight tube profiles in a preprocessor step and are used as boundary values at the flow entrance in the pulsatile simulation. Assuming a kinematic blood viscosity $\nu = 0{\cdot}035\,\text{cm}^2\,\text{s}^{-1}$, the resulting dimensionless parameters are $Re = 300$, Womersley number $\alpha = 4{\cdot}8$ ($\alpha = (L_0/2)\sqrt{(\omega/\nu)}$) and Dean number $\kappa = 212$ ($\kappa = Re\sqrt{(L_0/2R)}$).

The mass transport calculation is based on the diffusion coefficient $D = 2{\cdot}75 \times 10^{-5}\,\text{cm}^2\,\text{s}^{-1}$ for oxygen in blood and a physical permeability factor $\beta = 2{\cdot}45 \times 10^{-4}\,\text{cm}^3\,\text{dyn}^{-1}\,\text{s}^{-1}$ in (10). The constant $\beta$ was chosen such that the diffusive flux at the flow entrance and for time $t/T_\text{p} = 0{\cdot}25$ (mean flow rate) matches a physiological arterial reference flux[23] $g_0 = 4{\cdot}82 \times 10^{-6}$ $\text{ml}\,\text{cm}^{-2}\,\text{s}^{-1}$ ($\beta = g_0/\tau_0 C_\text{d}$, where $\tau_0 = 7{\cdot}63\,\text{dyn}\,\text{cm}^{-2}$). The resulting Peclet number is $Pe = 3{\cdot}81 \times 10^5$. A constant physiological reference concentration $C_\text{D} = 2{\cdot}58 \times 10^{-3}\,\text{ml}\,\text{O}_2\,\text{cm}^{-3}$ is assumed at the inlet. The numerical solution of the steady transport equation subject to the steady velocity field is chosen as initial concentration field $C_0(\mathbf{x})$ in the pulsatile calculation.

The finite element subdivision of the inflow cross-section and in the curved tube region is shown in Figure 1. Because of perfect geometric symmetry, only one half of the tube is discretized and the appropriate boundary conditions for the flow and mass transport calculations are applied. The semicircle is divided into 388 elements and 190 layers are created for the whole flow domain, resulting in 73,332 trilinear elements and 79,990 nodes. The total number of unknowns is 393,292. For a periodic solution, five pulse cycles are calculated, where each cycle is divided into 96 implicit time steps. The maximum error in periodicity is less than 0·3% for the velocities and less than 0·5% for the concentration. The solution of the linear equation systems uses a stabilized version of the bi-conjugate gradient method (BiCGSTAB)[24] for unsymmetric matrices and incomplete LU factorization for preconditioning.[25] Applying a compact storage scheme,[25] only non-zero components of the system matrices are stored in the form of a one-dimensional array. Using the solution vector of the last time step (iteration step) as a start vector for the BiCG solver, three to four iterations for the velocity components and two iterations for the concentration have to be carried out on average, where the criterion for the updated residual vector $\mathbf{r}$ was $\|\mathbf{r}\|_2/\|\mathbf{b}\|_2 < 10^{-7}$ ($\mathbf{b}$ is the right-hand side of the linear equation system).

Figure 2(a) shows axial velocity profiles in the symmetry plane and contour lines of axial velocity at cross-sections S1 and S2 (as indicated) for the pulse phase angle of maximum flow. Generally there

 

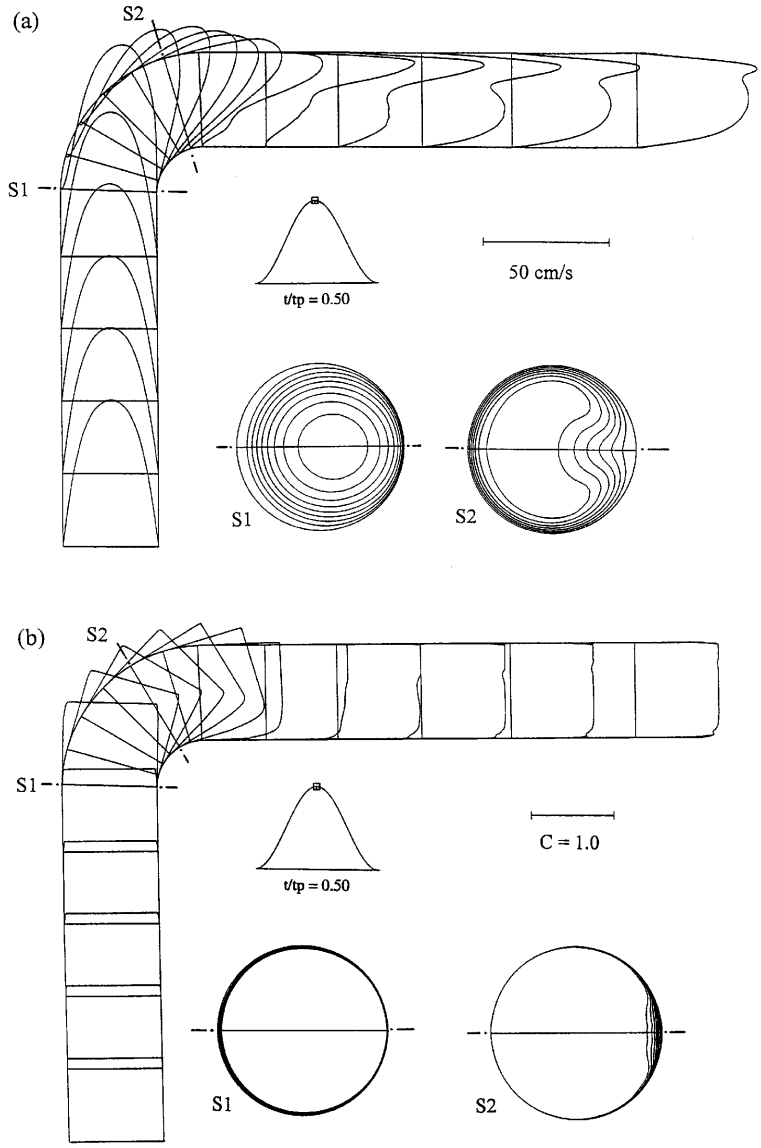


Figure 2. (a) Axial velocity profiles and contour lines of axial velocity. (b) Normalized concentration profiles and isoconcentration lines

are high velocity gradients at the outer wall and low velocity gradients at the inner wall of the bend. A small zone of reversed flow can be seen at the beginning of the curved section at the outer wall. Figure 2(b) demonstrates the corresponding profiles of normalized concentration $C/C_D$ and the isoconcentration contours. The concentration profiles have a blunted shape and are characterized by a small concentration boundary layer due to the high Peclet number. The isoconcentration contours demonstrate the widening of the concentration boundary layer at the inner side of the bend.

The wall shear stress $\tau_w$ along the outer wall and the inner wall at the symmetry plane is shown in Figure 3 for the pulse fractions $t/T_p = 0{\cdot}0$ (a), $0{\cdot}25$ (b), $0{\cdot}5$ (c), $0{\cdot}75$ (d) (the square symbols mark the

 

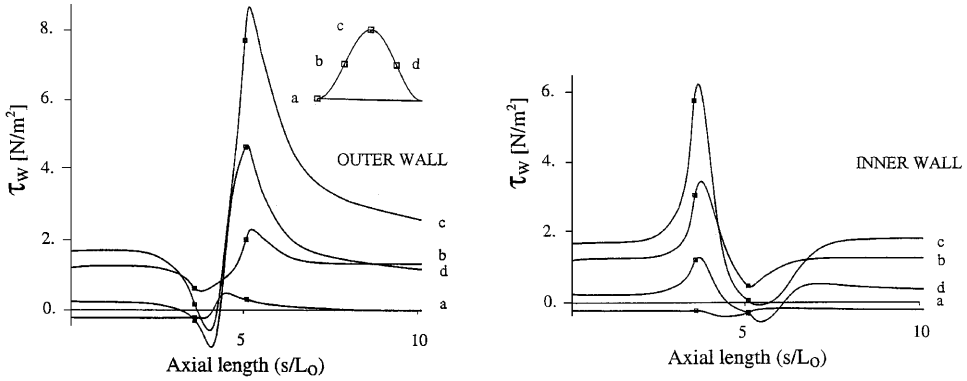


Figure 3. Wall shear stress $\tau_w$ along outer and inner walls of tube (symmetry plane) for different pulse phase angles (as indicated)

beginning and the end of the curved region). The maximum shear stress occurs at the outer wall at the end of the curved region (phase angle c). Reversed flow is indicated by negative shear stress values occurring at the outer wall at the beginning of the curved section and at the inner wall at the end of the curved section (phase angles c and d), where also the shear stress magnitude is low.

The influence of the wall shear stress on the non-dimensional diffusive wall flux $q_w$ (equation (8)) is demonstrated in Figure 4. Since the wall permeability $\alpha_w$ was assumed to be linearly dependent on the wall stress magnitude (equation (8)), the wall flux curves and the shear stress curves exhibit the same qualitative characteristic. According to clinical observations, atherosclerotic lesions in arterial bends preferentially occur at the inner wall at the end of the bend and at the outer wall at the beginning of the curved region. The numerical results show that there is a strong correlation with corresponding zones of low wall shear stress and low solute wall flux at these sites. The strong flux reduction in these regions results from both a wide concentration boundary layer (see Figure 2(a), position S1 and Figure 2(b), position S2) and a low wall permeability due to a low wall shear stress magnitude (Figure 3).

Figure 5 shows contours of the non-dimensional wall flux $q_w$ (equation (8)) and the normalized wall concentration on the surface of the tube for the pulse phase angle of maximum flow. The plot

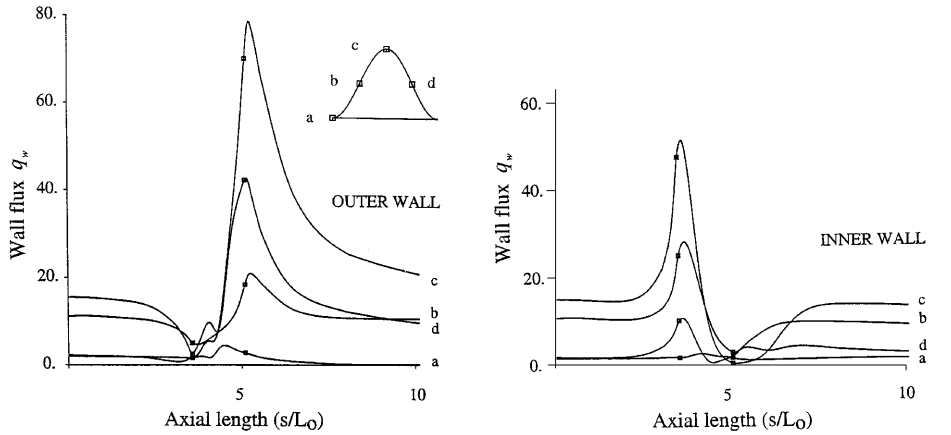


Figure 4. Non-dimensional wall flux $q_w$ at outer and inner walls of tube for different pulse phase angles (as indicated)

 

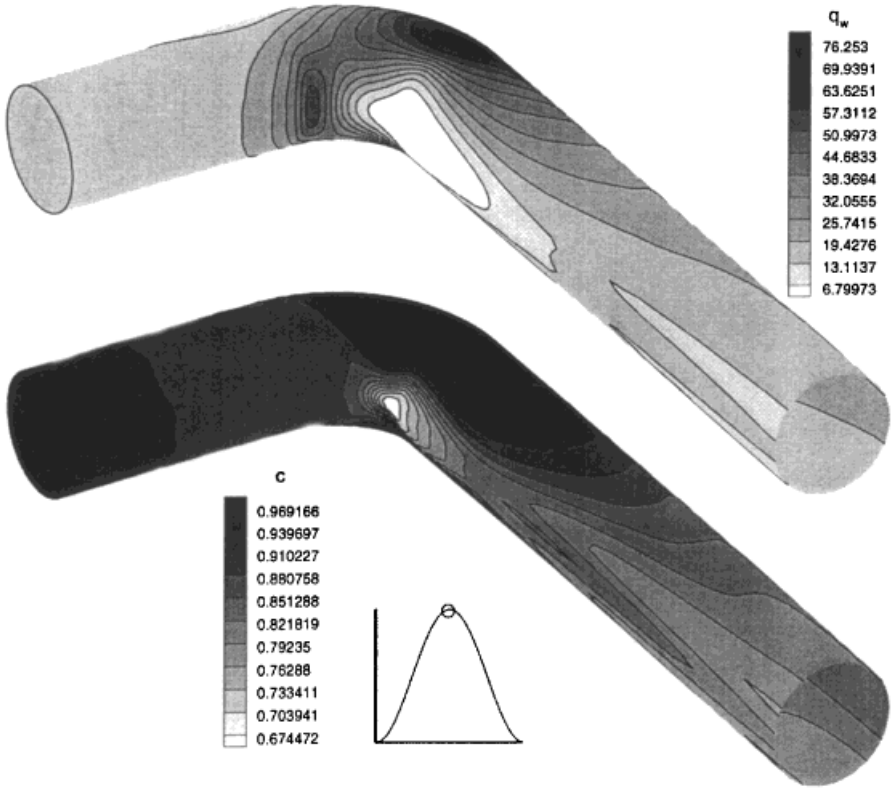


Figure 5. Contours of normalized wall flux (upper picture) and normalized wall concentration (lower picture) for pulse phase angle of maximum flow

demonstrates a severe wall flux reduction at the inner wall of the bend, where also the local wall concentration is low.

## 5. CONCLUSIONS

A numerical scheme for the simulation of unsteady blood flow and cardiovascular transport processes has been presented. The application of a streamline upwind/Petrov–Galerkin technique in the basic finite element formulations has enabled a stable solution of both the convection-dominated transport equations and the flow equations. The capability of treating simultaneously the blood phase transport and shear-dependent variations in wall permeability has been included in the model and is an important feature for the physiologically realistic modelling of arterial mass transfer processes.[1–5] Numerical results have been presented for 3D pulsatile mass transfer in an arterial bend. The main characteristic is a substantial wall flux reduction through the inner wall of the curvature in low-shear regions where the fluid boundary layer resistance is high and the wall permeability is low. This is in correlation with clinical observations of atherosclerotic lesions in low-shear regions at the inner wall of arterial bends.[26]

The linear shear-dependent permeability model used yielded a wall flux distribution exhibiting as much spatial variability as the wall shear stress itself. Although this simple model may not be valid

 

for oxygen transfer through the wall in this strong form, it principally demonstrates the effect of shear-dependent variations in intimal permeability on the wall flux distribution in a 3D numerical analysis. The consideration of shear-dependent endothelial permeability is very important in the mass transport of macromolecules such as albumin or LDL.[1] The development and experimental validation of models describing shear-dependent arterial wall permeability to macromolecules are a current objective of research.[27] On the basis of the presented stable numerical techniques and in combination with experimental data on wall permeability, it should be possible to carry out 3D numerical model studies on macromolecule transport.

ACKNOWLEDGEMENT

This study is supported by the Austrian Science Foundation, Project P 10494 TEC, Vienna, Austria.

REFERENCES

1. H. Jo, R. O. Dull, T. M. Hollis and J. M. Tarbell, 'Endothelial albumin permeability is shear dependent, time dependent and reversible', *Am. J. Physiol.*, **260**, H1992–H1996 (1991).
2. K. Perktold, M. Resch and H. Florian, 'Pulsatile non-Newtonian flow characteristics in a three-dimensional human carotid bifurcation model', *Trans. ASME, J. Biomech. Eng.*, **113**, 464–475 (1991).
3. K. Perktold and G. Rappitsch, 'Mathematical modeling of arterial flow and vessel mechanics', in J. M. Crolet and R. Ohayon (eds), *Computational Methods for Fluid–Structure Interaction*, PRNM Vol. 306, Longman, London, 1994, pp. 230–245.
4. K. Perktold and G. Rappitsch, 'Computer simulation of local blood flow and vessel mechanics in a compliant carotid artery bifurcation model', *J. Biomech.*, **28**, 845–856 (1995).
5. C. G. Caro, J. M. Fitzgerald and R. C. Schroter, 'Atheroma and wall shear: observation, correlation and proposal of a shear dependent mass transfer mechanism of atherogenesis', *Proc. R. Soc. Lond.*, **177**, 109–159 (1971).
6. L. H. Back, J. R. Radbill and D. W. Crawford, 'Analysis of oxygen transport from pulsatile, viscous blood flow to diseased coronary arteries of man', *J. Biomech.*, **10**, 763–774 (1977).
7. P. Ma, X. Li and D. N. Ku, 'Heat and mass transfer in a separated flow region for high Prandtl and Schmidt numbers under pulsatile conditions', *Int. J. Heat Mass Transfer*, **37**, 2723–2736 (1994).
8. G. Rappitsch and K. Perktold, 'Computer simulation of convective diffusion processes in large arteries', *J. Biomech.*, **29**, 207–215 (1996).
9. A. N. Brooks and T. J. R. Hughes, 'Streamline upwind/Petrov–Galerkin formulations for convection dominated flows with particular emphasis on the incompressible Navier–Stokes equations', *Comput. Methods Appl. Mech. Eng.*, **32**, 199–259 (1982).
10. T. E. Tezduyar and T. J. R. Hughes, 'Finite element formulations for convection dominated flows with particular emphasis to the compressible Euler equations', *AIAA Paper 83-0125*, 1983.
11. T. J. R. Hughes, M. Mallet and A. Mizukami, 'A new finite element formulation for computational fluid dynamics: II. Beyond SUPG', *Comput. Methods Appl. Mech. Eng.*, **54**, 341–355 (1986).
12. K. Perktold, 'Numerische Lösung des instationären dreidimensionalen Navier–Stokes Problems', *Ber. Math. Stat. Sekt., Forschungsges. Joanneum, Graz, Nr. 255, 1985.*
13. K. Perktold, 'On numerical simulation of three-dimensional physiological flow problems', *Ber. Math. Stat. Sekt. Forschungsges, Joanneum Graz, Nr. 280, 1987.*
14. P. Helin and I. Lorenzen, 'Arteriosclerosis in rabbit aorta induced by systematic hypoxia', *Angiology*, **20**, 1–12 (1969).
15. A. J. Chorin, 'Numerical solution of the Navier–Stokes equations', *Math. Comput.*, **22**, 745–762 (1968).
16. P. M. Gresho, S. T. Chan, R. L. Lee and C. D. Upson, 'A modified finite element method for solving the time-dependent incompressible Navier–Stokes equations. Part 1, Theory', *Int. j. numer. methods fluids*, **4**, 557–598 (1984).
17. J. Donea, S. Giuliani, H. Laval and L. Quartapelle, 'Solution of the unsteady Navier–Stokes equations by a finite element projections method', in *Computational Techniques in Transient and Turbulent Flow*, Pineridge, Swansea, 1981, pp. 97–132.
18. R. Temam, *Navier–Stokes Equations*, North-Holland, Amsterdam, 1979.
19. H. G. Girault and P. A. Raviart, *Finite Element Methods for Navier–Stokes Equations*, Springer, Berlin, 1980.
20. D. Hilbert, 'Ein Finite Elemente-Aufspaltungsverfahren zur numerischen Lösung der Navier–Stokes-Gleichungen und seine Anwendung auf die Strömung in Rohren mit elastischen Wänden', *Ph.D. Thesis*, Technical University Graz, 1987.
21. G. Rappitsch, 'Stable finite element methods for convection-dominated diffusion processes and application to cardiovascular transport problems', *Ph.D. Thesis*, Technical University Graz, 1996 (in German).
22. G. Rappitsch and K. Perktold, 'Pulsatile albumin transport in large arteries: a numerical simulation study', *J. Biomech. Eng.*, **118**, 511–519 (1996).

 

23. M. H. Friedman and L. W. Ehrlich, 'Effect of spatial variations in shear on diffusion at the wall of an arterial branch', *Circul. Res.*, **37**, 446–454 (1975).
24. H. A. Van der Vorst, 'Bi-CGSTAB: a fast and smoothly converging variant of Bi-CG for the solution of non-symmetric linear systems', *SIAM J. Sci. Stat. Comput.*, **13**, 631–644 (1992).
25. M. Hofer and K. Perktold, 'Vorkonditionieerter konjugierter Gradientenalgorithmus für große schlecht konditionierte unsymmetrische Gleichungssysteme', *Z. Angew, Math. Mech.*, **75**, S641–S642 (1995).
26. B. Fox, K. James, B. Morgan and A. Seed, 'Distribution of fatty and fibrous plaques in young human coronary arteries', *Atherosclerosis*, **41**, 337–347 (1982).
27. M. H. Friedman and D. L. Fry, 'Arterial permeability dynamics and vascular disease', *Atherosclerosis*, **104**, 189–194 (1993).

 